




ORIGINAL RESEARCH PAPER

Multi-objective optimisation of the HSPMM rotor based on the multi-physics surrogate model

Rui Dai¹  | Yue Zhang²  | Tianyu Wang³ | Fengge Zhang¹  | Chris Gerada⁴ | Yuan Zhang⁵

¹School of Electrical Engineering, Shenyang University of Technology, Shenyang, China

²School of Electrical Engineering, Shandong University, Jinan, China

³Department of Mechanical Engineering, Shenyang Institute of Engineering, Shenyang, China

⁴Power Electronics Machine and Control Group, University of Nottingham, Nottingham, UK

⁵Shandong Ou Ruian Electric Co. Ltd., Qingdao, China

Correspondence

Yue Zhang, School of Electrical Engineering,
Shandong University, 27 Shanda South Road, Jinan,
Shandong, China.
Email: yzhang35@sdu.edu.cn

Funding information

National Natural Science Foundation of China,
Grant/Award Numbers: 51920105011, 52077121

Abstract

High-speed permanent magnetic machine (HSPMM) is attracting more attention due to its high power density, compact size, small rotating inertia, and rapid response capability. However, the design of the HSPMM rotor is a non-linear, multi-physics coupled process that makes it difficult to build an accurate mathematical model for optimisation. This study proposes a multi-objective optimisation method based on the multi-physics surrogate model (MPSM). This method uses an MPSM to replace the finite element model (FEM) for optimisation, which can effectively solve the problem of non-convergence and time consumption of the traditional FEM in the optimisation process. Finally, a 1.1 MW, 18,000 r/min HSPMM is produced and related experiments are carried out; the feasibility of the method proposed in this study for HSPMM optimisation is verified.

KEYWORDS

AC machines, AC motors, optimisation, permanent magnet motors

1 | INTRODUCTION

High-speed permanent magnetic machine (HSPMM) is gaining popularity in the industry due to its high power density, compact size, small rotating inertia, and rapid response capability [1, 2]. It has been extensively used in applications such as electric vehicles, high-speed railways, air compressors, gas turbines, flywheels, and so on [3, 4]. Nevertheless, HSPMM will produce unique challenges due to the characteristics of high speed and high frequency [5–7].

The design of HSPMM is a typically non-linear, multi-physics design process that makes it difficult to build an accurate mathematical model for optimisation [8, 9]. At present, the design of HSPMM is mostly based on the multi-physics serial design of the finite element model (FEM), which is difficult to converge and

time consuming, especially for HSPMM optimisation because of multiple FEM calls. In [10], multi-physics optimisation based on the FEM for the HSPMM is proposed, which dramatically increases the optimisation time because of the use of a FEM at every function call. Multi-objective optimisation for the HSPMM based on the response surface method (RSM) is presented in [11]; however, the RSM is not suitable for handling highly non-linear problems such as the HSPMM design due to the insufficiency of the polynomial itself in expression.

In recent years, surrogate model (SM) technology has been extensively used in the field of multidisciplinary design [12]. The SM can express the relationship between a set of input variables and output variables through a mathematical model [13–15]. Under the action of the correlation function, the SM has the characteristics of local estimation, which makes it easy to obtain

This is an open access article under the terms of the Creative Commons Attribution-NonCommercial-NoDerivs License, which permits use and distribution in any medium, provided the original work is properly cited, the use is non-commercial and no modifications or adaptations are made.

© 2021 The Authors. *IET Electric Power Applications* published by John Wiley & Sons Ltd on behalf of The Institution of Engineering and Technology.

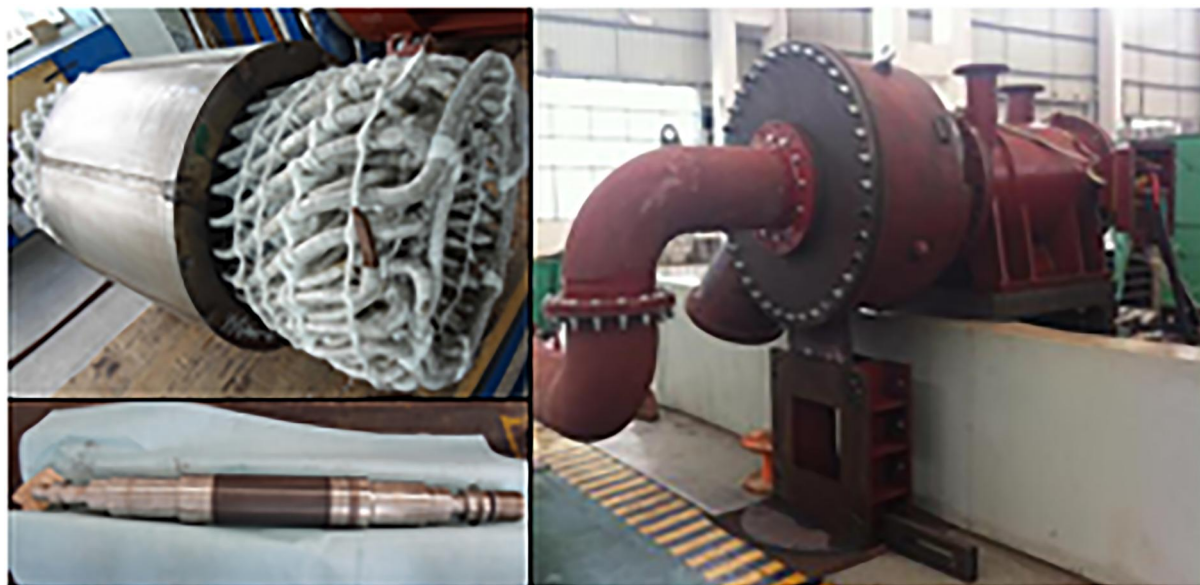


FIGURE 1 The prototype of the high-speed permanent magnetic machine

ideal fitting results when solving highly non-linear problems [16]. In [17], the SM is used to optimise the maximum output power of a doubly fed induction generator (DFIG). The SM is used to optimise the air gap flux density waveform of the flywheel energy storage machine in [18]. Hence, the SM can replace the complex FEM on the premise of meeting the approximate accuracy requirements, which can reduce the calculation cost and enhance the global optimisation rate.

This study proposes a multi-objective optimisation for the HSPMM based on the multi-physics surrogate model (MPSM), which is different from the conventional FEM optimisation. The biggest advantage is that the established MPSM is used in the optimisation process to replace the FEM model, which can effectively solve the problem of time consumption and convergence difficulties in the optimisation process caused by frequently calling the FEM in the optimisation process. The experimental prototype is shown in Figure 1, and its basic parameters are given as shown in Table 1. First, the multi-physics orthogonal sampling method is used to obtain initial sample points for MPSM establishment. Then, to verify the accuracy of the MPSM proposed in this study, an error analysis is performed to ensure approximate accuracy. Furthermore, the FEM is replaced by the MPSM to optimise the design using the Non-dominated Sorting Genetic Algorithm (NSGA-II). Finally, a 1.1 MW experimental prototype is developed, and the feasibility and effectiveness of the optimised design method based on the MPSM proposed in this study are verified through experimental research.

2 | CONSTRUCTION OF THE MPSM

Since electromagnetic, mechanical stress and rotor dynamics should be comprehensively considered in the HSPMM design process [19, 20], this will greatly increase the difficulty in the

TABLE 1 The basic parameters of the high-speed permanent magnetic machine

Parameter	Value	Unit
Rated power	1.1	MW
Rated voltage	3100	V
Rated speed	18,000	r/min
Rated frequency	600	Hz
Number of poles	4	-
Stator outer diameter	550	Mm
Stator inner diameter	190	Mm
Polar arc coefficient	0.75	-

design process. The traditional design process is generally based on the serial design of multi-physics, and the design process often needs to adjust the parameters according to the designer's experience, which is time-consuming and it is difficult to find an optimal solution. This study proposes a multi-objective optimisation method based on the MPSM, and the related flow diagram is presented in Figure 2.

2.1 | Definition of design parameters

In this study, permanent magnet (PM) material is generally fragile, hence a high-strength carbon fibre [26] is adopted to protect the PMs from damage due to the excessive centrifugal force. Reasonable design of the rotor of the HSPMM is crucial. In the design process, factors such as electromagnetic, mechanical stress and rotor dynamics need to be considered. Therefore, this study first assumes that the stator inner diameter, outer diameter, slot size, winding wire diameter, and number of turns are unchanged, and the rotor of the HSPMM

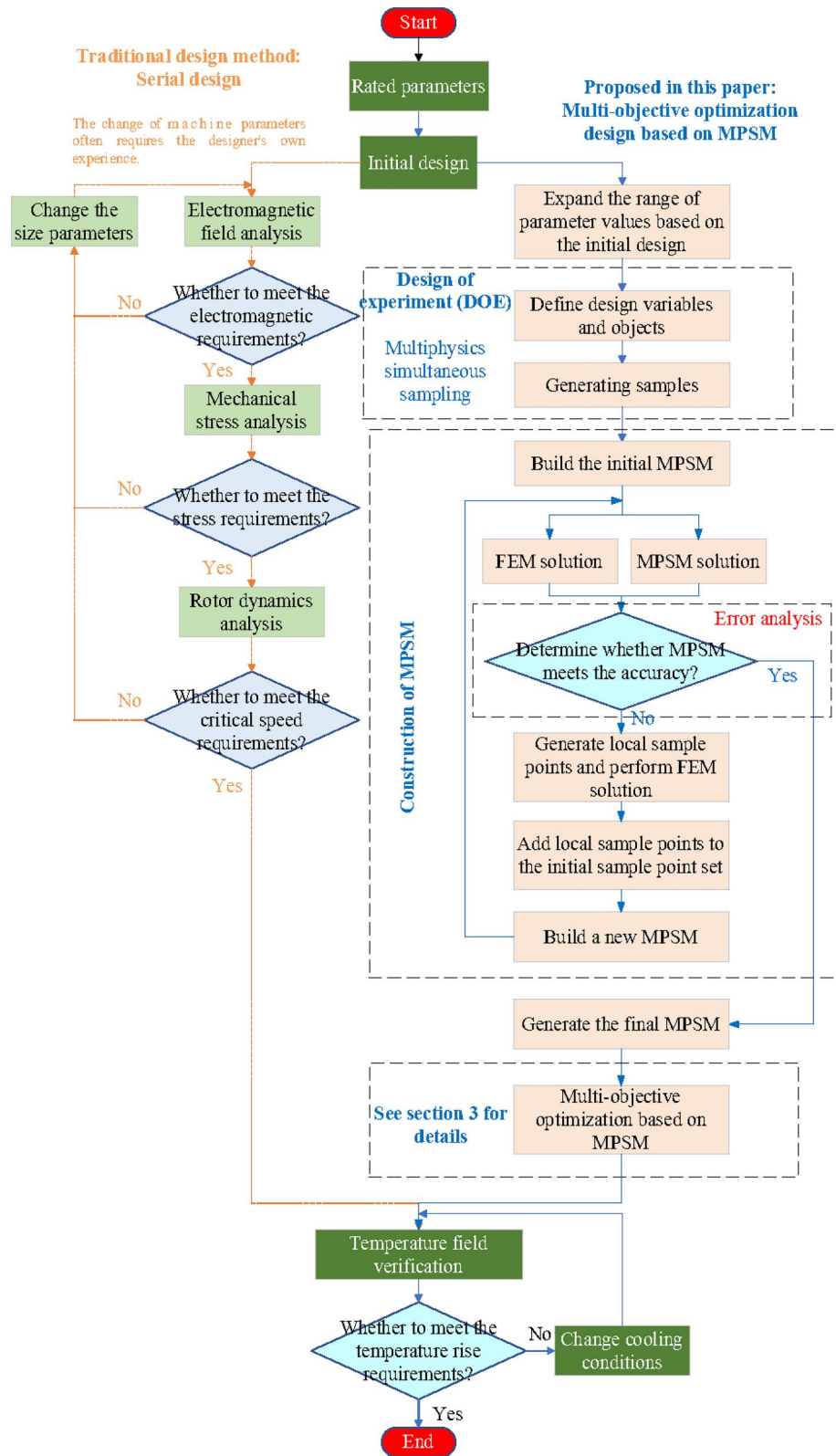


FIGURE 2 Optimal design process of the high-speed permanent magnetic machine based on the multi-physics surrogate model

is optimised. The design variables of the HSPMM are sleeve thickness (b_s), permanent magnet (PM) thickness (b_m), air gap size (δ), core effective length (l_{ef}), and interference fit (ϵ). The

upper and lower limits of the design variables are shown in Table 2, in which the scope of each variable is expanded based on the initial design.

In addition, the application of the surrogate model is similar to the black box principle. It only needs to pay attention to the relationship between the response variable and the input variable, not the specific process of the solution. This study comprehensively considers the physical field factors of the HSPMM; the response variables of the mechanical stress field are maximum radial stress of the PM at room temperature (σ_{rM}), maximum tangential stress of the PM at hot temperature ($\sigma_{\theta M(\text{thermal})}$), and maximum tangential stress of the sleeve at hot temperature ($\sigma_{\theta S(\text{thermal})}$), and minimum contact stress at room temperature (σ_c); the response variables of the electromagnetic field are no-load back EMF (E_0), air-gap magnetic density (B_{air}), output torque (T_{out}), and cogging torque (T_{cog}); the response variable of the dynamic is the first-order natural frequency (ω_{n1}).

2.2 | Design of experiment

The design of experiment (DOE) is a sampling plan in the design variable space [21], which aims at maximising the amount of information acquired and minimising the bias error. The balance between bias and variance errors shall be consulted during the construction of the MPSM.

TABLE 2 Design variables

Design variable	Symbol	Lower limit	Upper limit
Sleeve thickness (mm)	h_s	6	8
PM thickness (mm)	h_m	16	18
Air-gap length (mm)	δ	2	4
Core length (mm)	l_{ef}	390	410
Interference fit (mm)	ϵ	0.05	0.2

Abbreviation: PM, permanent magnet.

TABLE 3 $L_{64}(4^5)$ orthogonal table

	Input variables					Response variables									
Test number	h_m (mm)	h_s (mm)	δ (mm)	ϵ (mm)	l_{ef} (mm)	σ_{rM} (MPa)	$\sigma_{\theta M(\text{thermal})}$ (MPa)	$\sigma_{\theta S(\text{thermal})}$ (MPa)	σ_c (MPa)	ω_{n1} (Hz)	E_0 (V)	B_{air} (T)	T_{out} (N·m)	T_{cog} (mN·m)	
1	16	6	2	0.05	390	27.719	90.695	330.05	0.891	348	3197.05	0.631	602.36	459.528	
2	16	6	2	0.2	395	13.29	79.367	536.37	15.82	346.5	3239.32	0.636	604.26	465.652	
3	16	6	4	0.05	390	27.11	87.541	329.44	1.598	346.7	2929.18	0.575	561.4	572.95	
4	16	6	4	0.2	395	12.311	76.557	542.06	17.14	348	2892.07	0.574	558.04	565.813	
5	16	6.5	2	0.1	400	22.267	84.629	394.34	8.706	345	3197.49	0.614	599.8	505.509	
...															
60	18	7	3	0.2	395	11.903	71.408	532.24	21.793	345.75	3036.40	0.594	582.1	633.111	
61	18	8	2.5	0.1	410	22.872	77.525	385.47	11.872	341.17	3079.63	0.581	579.2	675.954	
62	18	8	2.5	0.15	400	16.645	73.702	449.56	19.203	343.9	3003.31	0.581	570.47	659.187	
63	18	8	3	0.1	400	22.754	77.563	385.5	12.899	343.67	2935.01	0.569	560.02	673.231	
64	18	8	3	0.15	410	17.247	72.094	448.46	17.197	341.07	3009.63	0.569	568.89	690.387	

Generally, the bias error can be lowered through a DOE by distributing the sample points uniformly in the design space.

Within the above design range, an orthogonal test design is utilised to generate an initial sample point, as shown in Table 3, which has four levels and five factors.

The data in Table 3 are analysed for the interaction and main effect, and the results are shown in Figures 3 and 4, respectively. It can be seen from Figure 3 that there is an interaction between multiple design variables, where the larger the crossing angle, the more obvious is the interaction. It can be seen from Figure 4 that the larger the slope, the more noticeable the main effect on the response variable. Among them, the x-axis 'low' represents the minimum value of each design variable, and 'high' represents the maximum value of each design variable.

2.3 | Surrogate model establishment

In this study, the Kriging model is mainly used to establish the MPSM, which is used to determine the value of the regional change in a limited area based on the correlation and variability of the variables.

The Kriging model can be written in the following mathematical form [22, 23]:

$$y = f(x) = g(x) + z(x) \quad (1)$$

where $g(x)$ is a deterministic part, called deterministic drift. In the design space, it provides a global approximation to the simulation, which is generally expressed by a polynomial of x , $z(x)$ is called fluctuation, which provides an approximation to the simulated local deviation, and has the following characteristics:

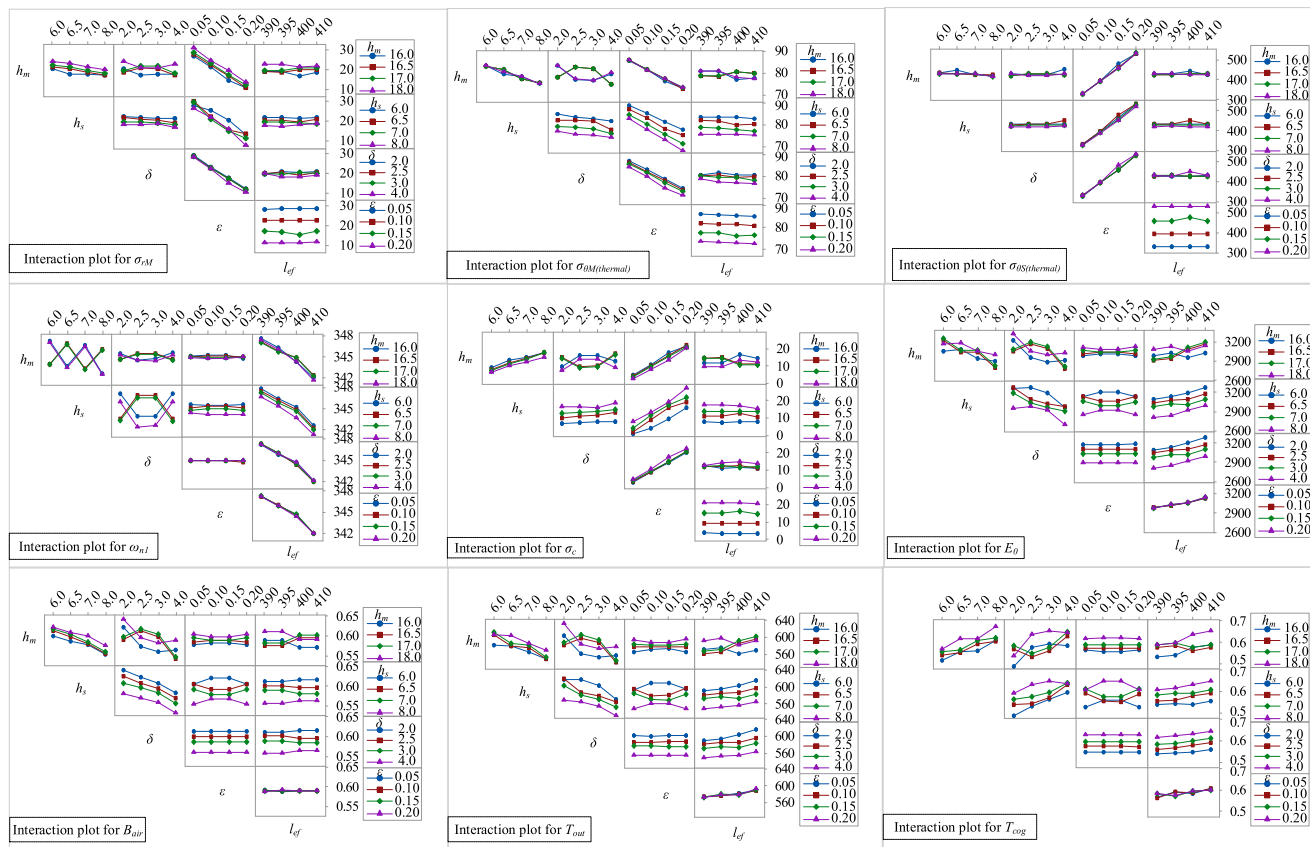


FIGURE 3 Interaction plot for the response variables

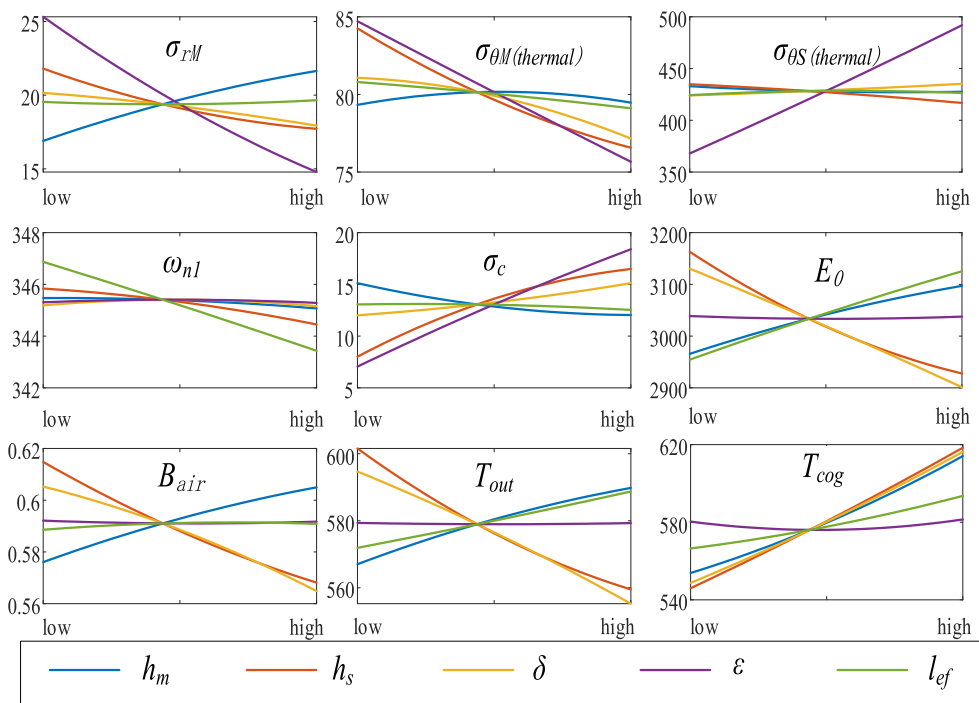


FIGURE 4 Main effect plot

$$\begin{cases} E[z(x)] = 0 \\ \text{var}[z(x)] = \sigma^2 \\ \text{cov}[z(x), z(x^i)] = \sigma^2 R(c, x, x^i), i = 1, 2, \dots, n \end{cases} \quad (2)$$

where x^i is the input part of the i th training sample point; n is the number of sample points; and $R(c, x, x^i)$ is a correlation function with c as a parameter. This study takes the exponential function as the correlation function, and its expression is as follows:

$$R(c, x, x^i) = \prod_{j=1}^m \exp\left(-\frac{|x_j - x_j^i|}{c_j}\right) \quad (3)$$

where c_j is the constant parameter of the function in the j th direction of the sample point; m is the dimension of the sample point; x_j is the coordinate of the point to be measured in the j th direction, x_j^i is the coordinate of the i th sample point in the j th direction. According to the above statistical characteristics,

$$E[f(x)] = g(x) \quad (4)$$

Use the linear weighted superposition interpolation of the response value y^i of the sample point x^i to calculate the response value of the measured point x :

$$\begin{cases} \hat{f}(x) = w^T Y \\ w = [\omega_1, \omega_2, \omega_3, \dots, \omega_n]^T \\ Y = [Y_1, Y_2, Y_3, \dots, Y_n]^T \end{cases} \quad (5)$$

At this time, the unbiased condition needs to be met, namely

$$E[w^T Y - f(x)] = w^T G - g(x) = 0 \quad (6)$$

and then get

$$G^T w = g(x) \quad (7)$$

where $G^T = [g(x^1), g(x^2), \dots, g(x^n)]$, At this time, the prediction variance produced as a prediction model is as follows:

$$\begin{aligned} \varphi(x) &= E\left\{ [f^*(x) - f(x)]^2 \right\} \\ &= \sigma^2 (1 + w^T R_{ij} w - 2w^T r(x)) \end{aligned} \quad (8)$$

$$\begin{cases} R_{ij} = [R(c, x^i, x^j)] \quad (i, j = 1, 2, \dots, n) \\ r(x) = [R(c, x, x^1), \dots, R(c, x, x^n)]^T \end{cases} \quad (9)$$

Since the Kriging model requires the minimum prediction variance, the final result obtained by Lagrangian multiplication is as follows:

$$w = R_{ij}^{-1} \left\{ r(x) - G(G^T R_{ij}^{-1} G)^{-1} [G^T R_{ij}^{-1} r(x) - g(x)] \right\} \quad (10)$$

Substitute it back to (1) to get the following:

$$\begin{cases} \hat{f}(x) = g(x)\beta^* + r^T(x)\gamma^* \\ \beta^* = (G^T R_{ij}^{-1} G)^{-1} G^T R_{ij}^{-1} Y \\ \gamma^* = R_{ij}^{-1} (Y - G\beta^*) \end{cases} \quad (11)$$

Ensuring that other variables remain unchanged, this study uses h_s and ϵ as input variables to illustrate the MPSM prediction results in the stress field, uses h_m and δ as input variables to illustrate the MPSM prediction results in the electromagnetic field and uses h_m and l_{ef} as input variables to illustrate the MPSM prediction results of the first-order critical speed. The prediction results of each response variable are displayed in Figure 5. It can be seen from Figure 5a that the increase of sleeve thickness (h_s) and interference fit (ϵ) is beneficial to reduce the PM radial stress and the PM tangential stress, and it is also beneficial to increase the contact between the PM and the sleeve. However, the change of sleeve thickness (h_s) has little effect on sleeve tangential stress and can be ignored. Meanwhile, with the increase of the interference fit (ϵ), the sleeve tangential stress will increase sharply. It can be seen from Figure 5b that the no-load back-EMF (E_0), air gap flux density (B_{air}), output torque (T_{out}), and cogging torque (T_{cog}) of the HSPMM will all increase accordingly as the PM thickness (h_m) increases; as the air gap length (δ) increases, the no-load back-EMF (E_0), air gap flux density (B_{air}), and output torque (T_{out}) of the HSPMM decrease, but the cogging torque (T_{cog}) increases. It can be seen from Figure 5c that the PM thickness (h_m) has little effect on the first-order natural frequency (ω_{n1}), but the first-order natural frequency gradually decreases with the increase of the effective length (l_{ef}).

2.4 | Error analysis

The purpose of error analysis is to ensure that the constructed surrogate model can effectively express the information contained in the original model.

A cross-validation error analysis is used in this study. Several data points that are chosen randomly will be removed from the sampling data set, one at a time. For each of the removed points, the approximation coefficients will be recalculated, and the exact and surrogate output values will be compared. A total of 10 data points randomly selected from sampling points are used for cross-validation. Since there are not many data points used for cross-validation, leave-one-out cross-validation (Loo-CV) is used in this study. In these 10 sample points, each sample point is used as the verification set separately, and the remaining 9 sample points are used as the training set, and so on.

This study uses R -square (R^2) as the error index of the surrogate model. The closer R^2 is to 1, the more accurate is the surrogate model. Usually, the R^2 needs to be greater than 0.95. The R^2 can be expressed as follows:

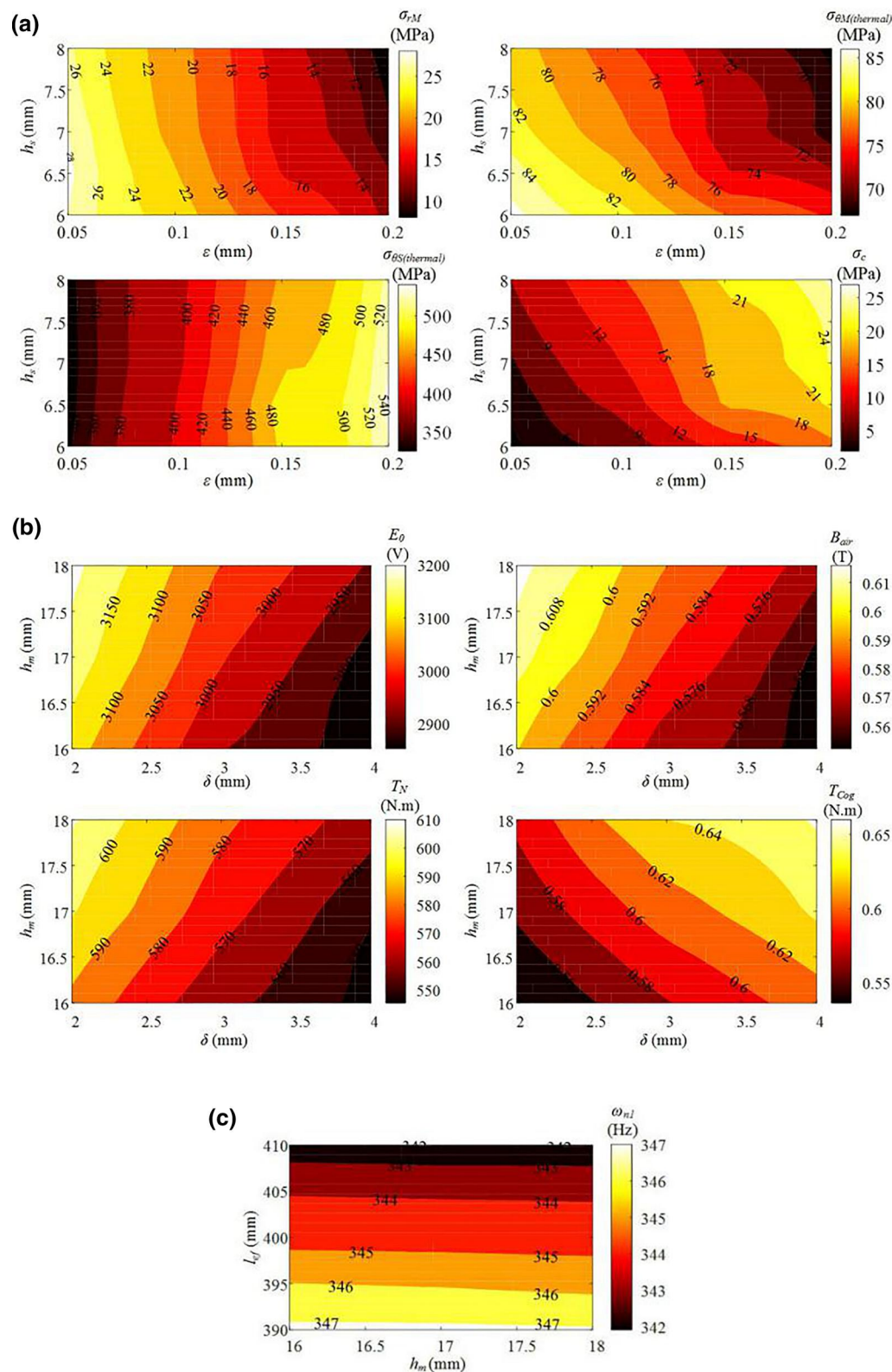


FIGURE 5 Multi-physics surrogate model predicted values of each physical field response variable: (a) predicted results of the stress field; (b) predicted results of the electromagnetic field; (c) prediction result of the first-order natural frequency

$$R^2 = 1 - \frac{SSE}{SSY} = 1 - \frac{\sum_{i=1}^N (f_i - \hat{f}_i)^2}{\sum_{i=1}^N (f_i - \bar{f})^2} \quad (12)$$

$$\begin{cases} SSE = \sum_{i=1}^N (f_i - \hat{f}_i)^2 \\ SSY = \sum_{i=1}^N (f_i - \bar{f})^2 = \sum_{i=1}^N f_i^2 - \frac{1}{N} \left(\sum_{i=1}^N \hat{f}_i \right)^2 \end{cases} \quad (13)$$

where N is the number of sample points in the test set, f_i is the calculated value of CFD, \hat{f}_i is the predicted value of the surrogate model, and \bar{f} is the surrogate mean of the sample points.

Figure 6 depicts the error analysis results of each response variable. It can be seen that the predicted values are close to the FEM actual values, and the R^2 values of the target variables are greater than 0.95. Furthermore, it proves that the surrogate model has a high degree of confidence.

3 | OPTIMISATION BASED ON THE MPSM

The FEM is replaced by the above MPSM to optimise the design. Due to the design of the HSPMM, it needs to consider a variety of objectives. This study chooses the NSGA-II as the optimisation method. In the NSGA-II, each objective

parameter is treated separately [24]. Standard genetic operation of mutation and crossover are performed on the designs. The selection process is based on two main mechanisms, ‘non-dominated sorting’ and ‘crowding distance sorting’. Each object is treated separately and the Pareto set is constructed by selecting feasible non-dominated designs. Figure 7 shows the optimisation flow diagram, where P_t is the parent population, Q_t is a sub-population of this generation, M_t is the combined population, P_{t+1} is the next generation of the parent population, and g is the number of iterations. In this study, the population size is 80, and the maximum number of iterations is 240, crossover probability is 0.9, and mutation probability is 0.1.

In the optimisation process of the HSPMM, the mechanical stress must meet the following three conditions: (1) the maximum stress of the sleeve must be less than the allowable stress of the material; (2) the maximum stress of the PM must be less than the allowable stress of the material; and (3) the contact stress between the PM and the rotating shaft must be guaranteed to be positive. (If it is negative, it means that the PM is disengaged from the shaft, and the torque will not be transmitted.)

For electromagnetic constraints, it is necessary to ensure that the no-load back-EMF of the motor is 0.9–1 times the rated voltage. The PM, air gap radial dimension, and the effective axial length are adjusted to limit the no-load back-EMF. Meanwhile, it is necessary to make sure that the output torque (T_{out}) of the motor is not lower than the rated torque (T_N). The air gap magnetic density value is adjusted between 0.5 and 0.7 T. The reason is that if the air gap

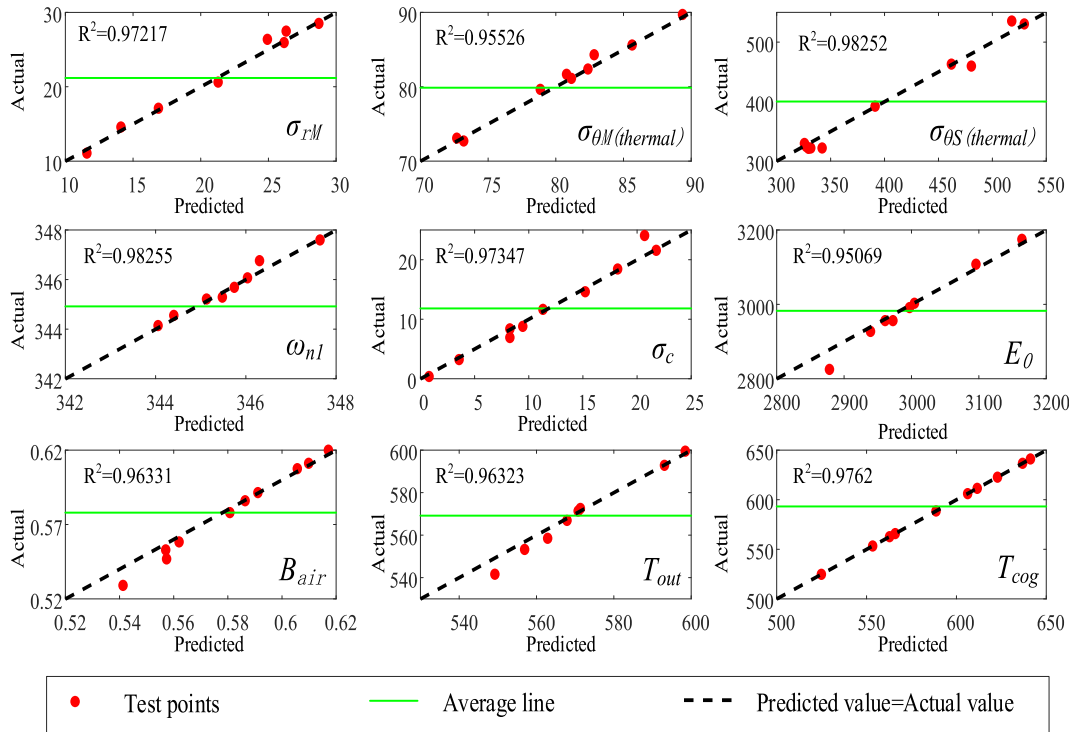


FIGURE 6 Error analysis results

magnetic density is too small, the motor will not produce enough output torque; if the air gap magnetic density is too large, the stator magnetic density will be too large, which will cause greater iron loss.

In order to avoid resonance of the rotor, the safety margin between the operating speed and the bending whirling critical speed needs to be larger [25], and the safety margin of this study is 15%.

According to the previous analysis, the mathematical model of the rotor optimisation problem for the HSPMM can be described as follows:

$$\begin{cases} G(Z) = \min \{ \sigma_{rM}; \sigma_{\theta M(\text{thermal})}; \sigma_{\theta S(\text{thermal})}; 1/\sigma_c; 1/\omega_{n1}; T_{\text{cog}} \} \\ \text{s.t. } Z = (b_s, b_m, \delta, l_{ef}, \varepsilon) \\ F_1 < 1000 \text{ MPa} \\ F_2 < 80 \text{ MPa} \\ \sigma_c > 0 \text{ MPa} \\ 0.9U_N < E_0 < U_N \\ T_{\text{out}} \geq T_N \\ 0.5T < B_\delta < 0.7T \\ (\omega_{n1} - \omega_e) > 0.15\omega_e \end{cases} \quad (14)$$

According to the main effect diagram above, two main optimisation parameters are selected to illustrate the optimisation process of the method proposed in this study, as shown in Figure 8. Among them, the red points are the infeasible points in the optimisation process, and the blue points are the feasible points in the optimisation process. It can also be seen that this method has better global optimisation capabilities.

Figure 9 shows the Pareto front of the optimisation based on the MPSM proposed in this study. It can be observed from Figure 9 that the optimisation method based on the MPSM used in this study can obtain a set of Pareto solution sets with relatively uniform distribution, which can provide designers with more feasible design solutions. Taking into consideration the problems of machining, the final optimisation scheme and its corresponding calculation results are shown in Table 4.

4 | MPSM OPTIMISATION SCHEME ANALYSIS AND THERMAL CALCULATION

In order to further verify the feasibility of the machine design method based on the MPSM, multi-physics performance analysis and thermal calculations are performed on the optimisation scheme in this section.

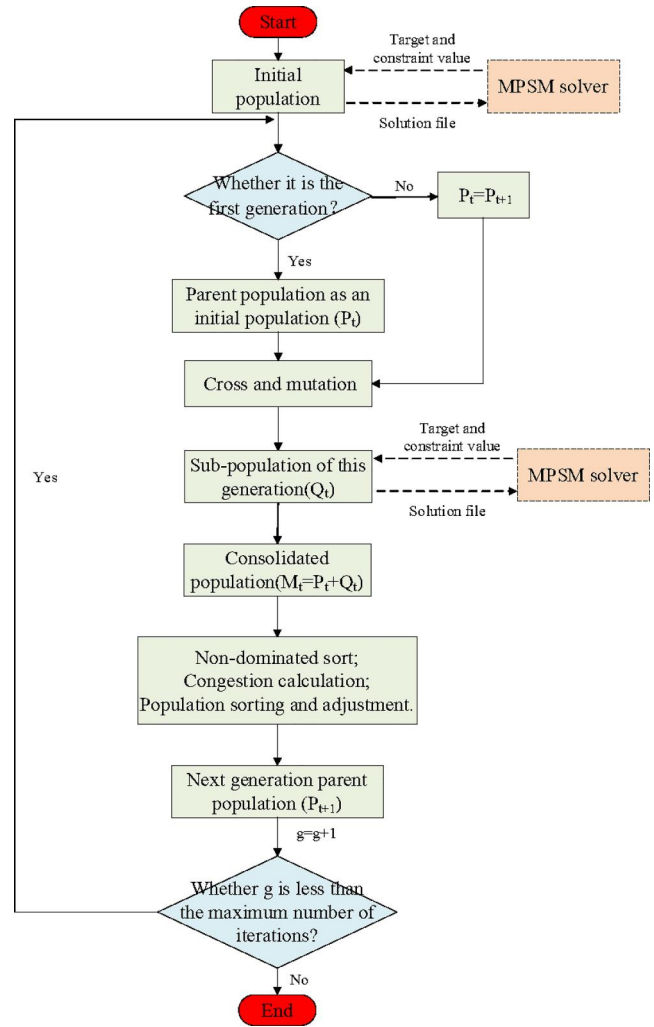


FIGURE 7 Optimisation flow diagram

4.1 | Electromagnetic field analysis

The electromagnetic field analysis result based on the FEM is shown in Figure 10. It can be seen that the magnetic field distribution is reasonable, the back-EMF is sinusoidal and its RMS value is about 3.04 kV, and the average air gap magnetic density is 0.58 T. Their values are consistent with the values calculated by the optimisation scheme based on the MPSM proposed in this study and has high credibility.

4.2 | Mechanical stress analysis

Figure 11 illustrates the rotor stress and contact stress distribution at the rated speed. It can be seen from Figure 11 that the maximum PM radial stress at normal temperature and the maximum tangential stress at hot temperature are 18.8 and 78 MPa, respectively. The maximum sleeve tangential stress at hot temperature is 517.8 MPa, and the minimum PM contact stress is 16 MPa. The calculated value of the FEM is basically consistent with the calculated value of the optimisation method.

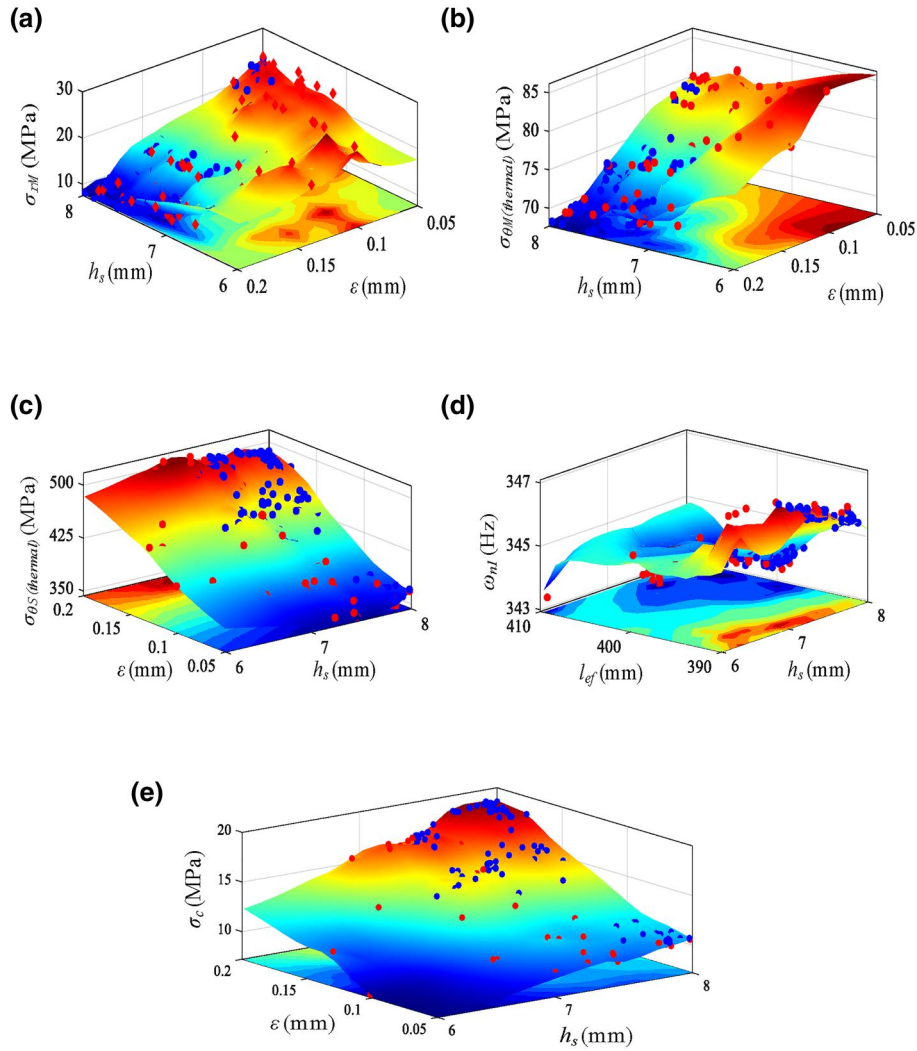


FIGURE 8 The optimisation process based on the MPSM: (a) σ_{TM} versus ϵ and h_s ; (b) $\sigma_{\theta M(thermal)}$ versus ϵ and h_s ; (c) $\sigma_{\theta S(thermal)}$ versus ϵ and h_s ; (d) ω_{n1} versus h_s and l_{ef} ; (e) σ_c versus ϵ and h_s

based on the MPSM in Table 4, which proves the reliability of the optimisation method proposed in this study.

4.3 | Rotor dynamics analysis

In this study, the rotor dynamics is verified and analysed by the 3D finite element. Taking into account the gyro effect, the Campbell diagram of its modal frequency varying with the speed is shown in Figure 12. It can be observed that the first-order critical speed is about 20,735 r/min, which exceeds the rated speed by 15.19%. The corresponding first-order natural frequency is 345.58 Hz, which is basically consistent with the MPSM prediction in Table 4.

4.4 | Thermal calculation

The previous analysis can ensure the feasibility of the method proposed in this study in terms of the electromagnetic field,

stress field, and rotor dynamics. This section will verify the temperature field of the HSPMM. A hybrid cooling method of casing water cooling and rotor ventilation is adopted, and the temperature field is analysed by the fluid–solid coupling method. In order to improve the speed of the solution, considering the symmetry of the machine in the circumferential direction, the range of the stator slot distance of the HSPMM is selected for the 3D solution domain model. The boundary conditions of the calculation model can be considered as follows:

- (1) Inlet wind speed is 15 m/s. Outlet pressure is standard atmospheric pressure (0.101325 MPa).
- (2) The convection heat transfer coefficient needs to be given for the water channel surface.
- (3) Inlet water temperature is assumed to be 20°C, and the heat transfer coefficient is 2600 W/m²/K.

The temperature distribution in the entire machine can be obtained as presented in Figure 13. It can be seen that

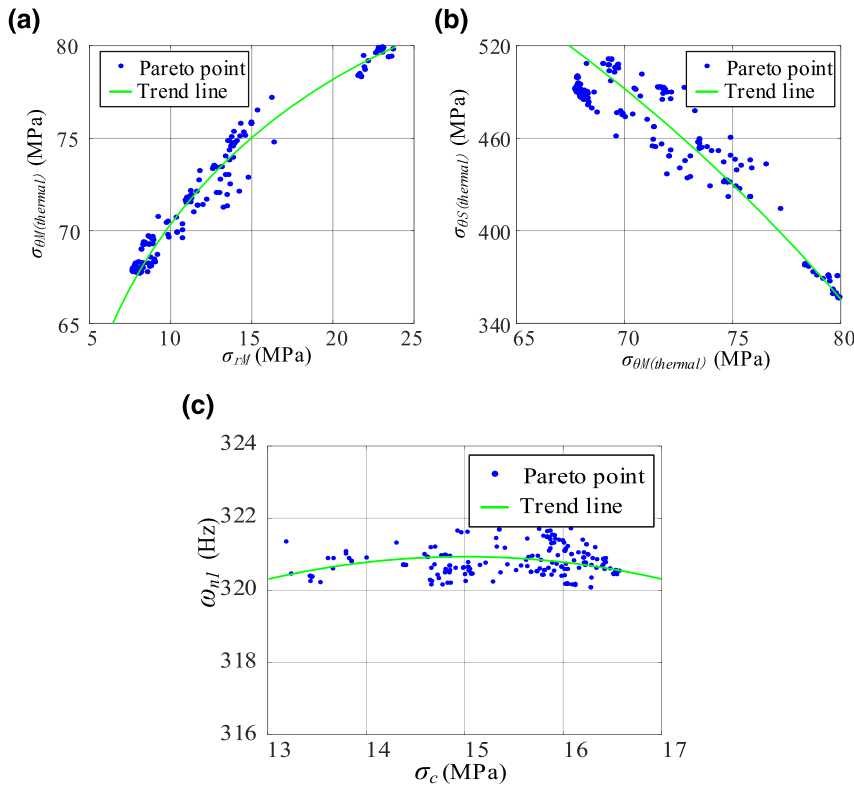


FIGURE 9 Pareto front of multi-objective (a) σ_{rM} and $\sigma_{\theta M(\text{thermal})}$, (b) $\sigma_{\theta M(\text{thermal})}$ and $\sigma_{\theta S(\text{thermal})}$, and (c) ω_{n1} and σ_c

the rotor maximum temperature is 143.3°C and appears in the middle of the rotor, which is less than the maximum working temperature of the material. Through the analysis of temperature characteristics, it is clear that the designed HSPMM can run safely under the rated operation conditions.

5 | EXPERIMENT

Based on the previous analysis, a 1.1 MW, 18,000 r/min HSPMM is manufactured. In order to ensure the rationality of the design method proposed in this study, the motor was tested experimentally. The no-load back-EMF is tested at the rated speed, and the result is displayed in Figure 14a. It can be seen that the RMS value of the no-load back-EMF is about 3.1 kV, which is very close to the rated voltage. The motor is powered by a variable frequency drive (VFD) with voltage. The VFD is a nine-level high-voltage inverter with the vector control method applied to achieve control in both machine speed and power during high-speed operation. The load current is illustrated in Figure 14b, and the RMS value is 235 A.

In addition, the trajectory of the spindle out of the front and rear bearings at the rated speed was tested, as shown in Figure 15. It can be seen from the figure that the peak-to-peak values in the x and y directions of the front bearing are 0.06753 and 0.05405 mm, respectively; the peak-to-peak values in the x - and y -directions of the rear bearing are 0.06650 and

TABLE 4 Optimisation results based on the multi-physics surrogate model

Optimisation variable	Value	
	Traditional method	Method of this study
b_m (mm)	18	17
b_s (mm)	8	7
δ (mm)	4	3.0
ε (mm)	0.1	0.18
l_{ef} (mm)	410	400
σ_{rM} (MPa)	4.61	18.89
$\sigma_{\theta M(\text{thermal})}$ (MPa)	70.8	78.1
$\sigma_{\theta S(\text{thermal})}$ (MPa)	449.9	516.66
σ_c (MPa)	5.3	15.89
E_0 (V)	3082.6	3088.96
B_{air} (T)	0.53	0.58
T_{out} (N·m)	610.1	609.5
T_{cog} (N·m)	0.71	0.606
ω_{n1} (Hz)	345.6	345.5

0.05962 mm, respectively. Hence, the motor will not have obvious vibration displacement during the rated operation, and the reliability of the design method proposed in this study can be guaranteed.

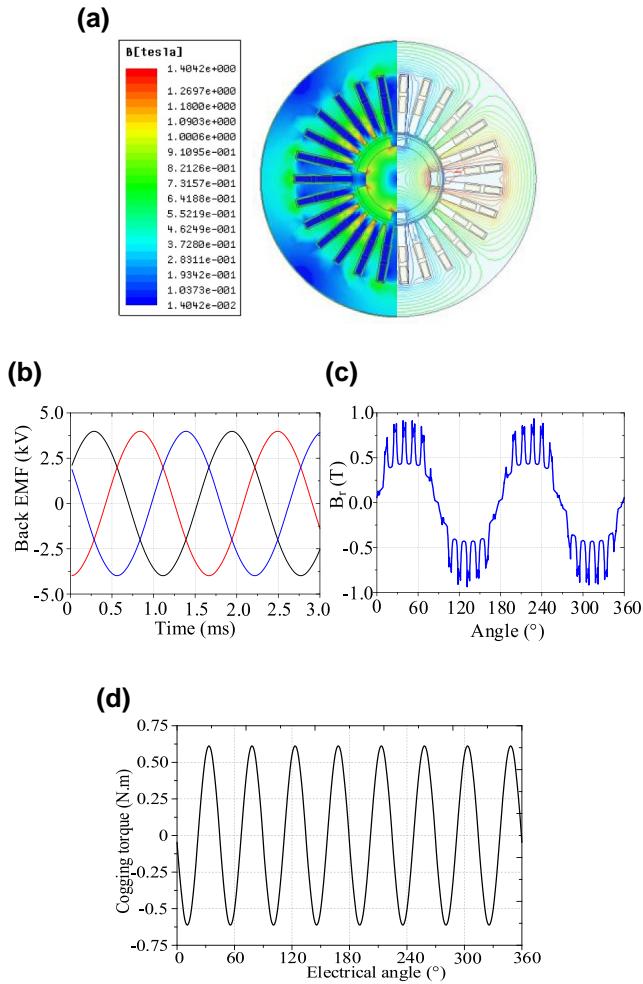


FIGURE 10 Electromagnetic performance of the high-speed permanent magnetic machine: (a) magnetic field distribution, (b) no-load back-EMF, (c) air-gap flux density, and (d) cogging torque

6 | CONCLUSION

The reasonable design of the PM rotor is the top priority of the HSPMM. In the rotor design process, it is necessary to integrate the electromagnetic field, stress field, rotor dynamics and temperature field. However, the design of the HSPMM rotor is a non-linear, multi-physics coupled process that makes it difficult to build an accurate mathematical model for optimisation. This study proposes a rotor optimisation method based on the MPSM. First, an orthogonal experiment is used to collect multi-physics sample points, and determine the main effects and interactions of the design variables. Second, an MPSM is constructed and its error analysis is performed to ensure its reliability. Then, the NSGA-II is used for multi-objective optimisation, and the final plan is verified by FEM calculation. Finally, a 1.1 MW, 18,000 r/min HSPMM is produced and related experiments are carried out; the feasibility of the method proposed in this study for HSPMM optimisation is further verified.

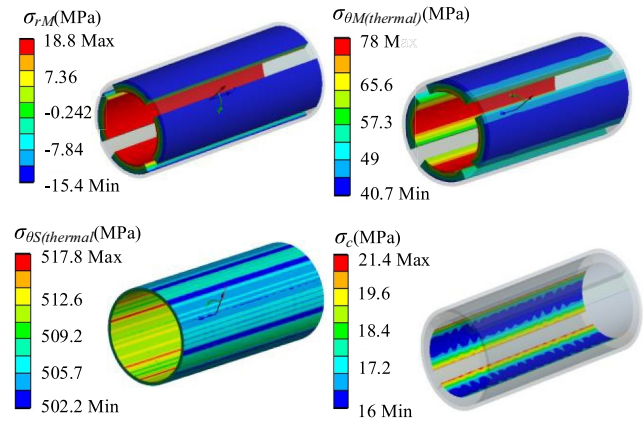


FIGURE 11 Rotor mechanical stress distribution

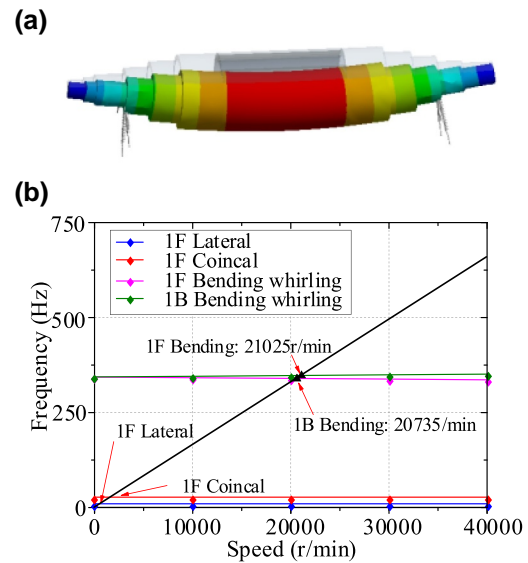


FIGURE 12 Rotor dynamic analysis: (a) first-order bending mode, (b) Campbell diagram

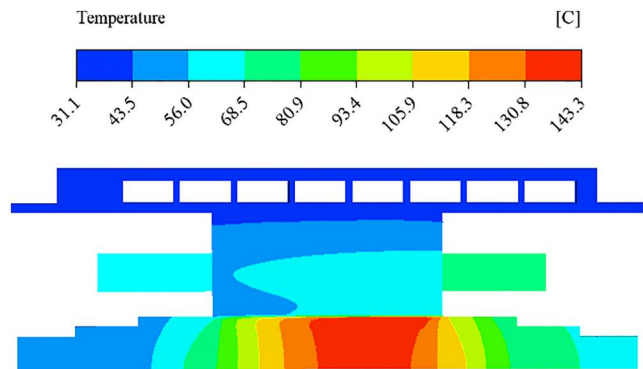


FIGURE 13 Temperature field analysis results

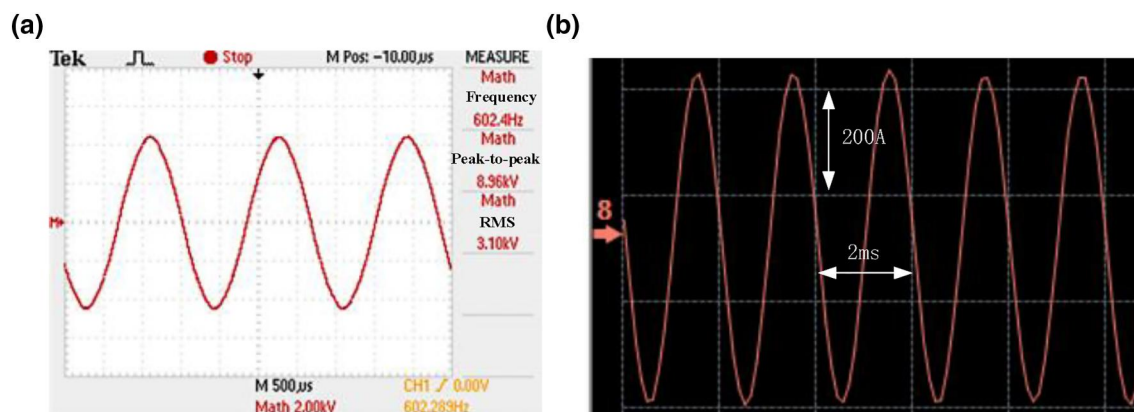


FIGURE 14 Experimental data: (a) no-load back EMF, (b) load current

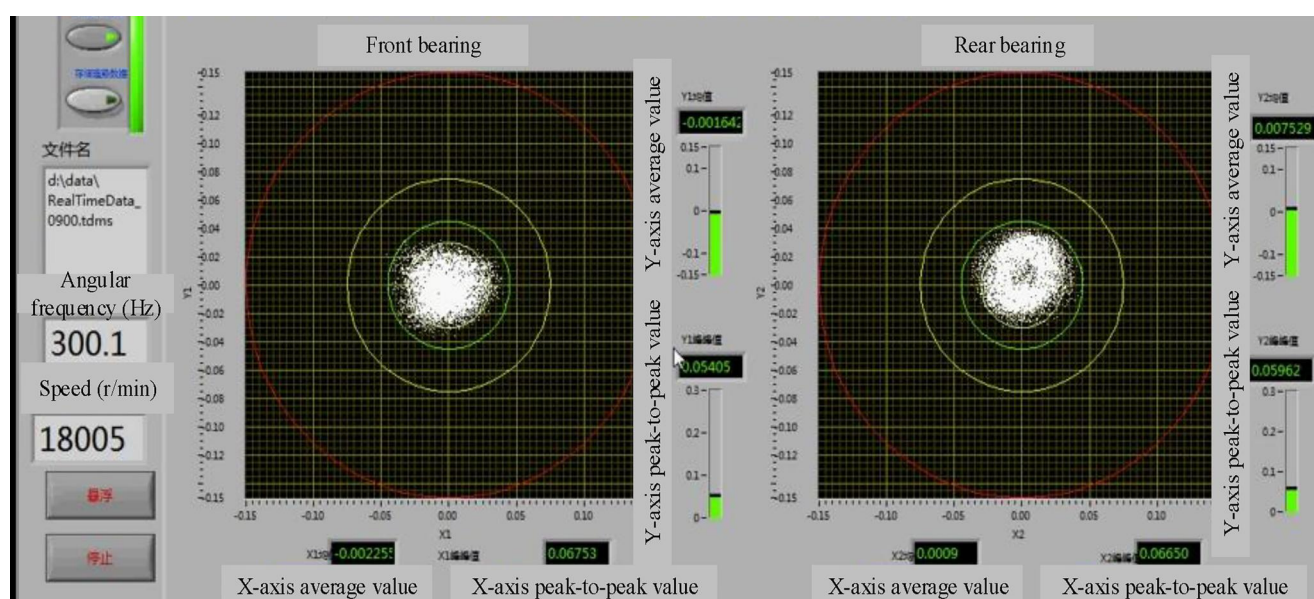


FIGURE 15 Rotor vibration displacement at the rated speed

ACKNOWLEDGEMENT

This work was supported by the National Natural Science Foundation of China under Grants 51920105011 and 52077121.

CONFLICT OF INTEREST

The authors declare no conflict of interests.

DATA AVAILABILITY STATEMENT

The data that support the findings of this study are available from the corresponding author upon reasonable request.

ORCID

Rui Dai <https://orcid.org/0000-0002-3239-7765>

Yue Zhang <https://orcid.org/0000-0003-4294-5849>

Fengge Zhang <https://orcid.org/0000-0002-1099-522X>

REFERENCES

1. Du, G., Huang, N.: Multiphysics analysis of high-speed permanent magnet generators for waste heat application. *IET Electr. Power Appl.* 14(6), 937–942 (2020)
2. Gerada, D., et al.: High-speed electrical machines: technologies, trends, and developments. *IEEE Trans. Ind. Electron.* 61(6), 2946–2959 (2014)
3. Dong, J., et al.: Review on high speed permanent magnet machines including design and analysis technologies. *Proc. CSEE.* 34(27), 4640–4653 (2014)
4. Kolondzovski, Z., et al.: Power limits of high-speed permanent-magnet electrical machines for compressor applications. *IEEE Trans. Energy Convers.* 26(1), 73–82 (2011)
5. Chen, L.-L., et al.: Rotor strength analysis for high-speed segmented surface-mounted permanent magnet synchronous machines. *IET Electr. Power Appl.* 12(7), 979–990 (2018)
6. Liu, G., et al.: High-speed permanent magnet synchronous motor iron loss calculation method considering multiphysics factors. *IEEE Trans. Ind. Electron.* 67(7), 5360–5368 (2020)

7. Jang, G.-H., et al.: Design and characteristic analysis of a high-speed permanent magnet synchronous motor considering the mechanical structure for high-speed and high-head centrifugal pumps. *IEEE Trans. Magn.* 54(11), 1–6 (2018)
8. Zhang, F., et al.: Design of HSPMM based on multi-physics fields. *IET Electr. Power Appl.* 12(8), 1098–1103 (2018)
9. Fang, H., et al.: Rotor design for high-speed high-power permanent-magnet synchronous machines. *IEEE Trans. Ind. Appl.* 53(4), 3411–3419 (2017)
10. Zhao, W., et al.: Multi-physics and multi-objective optimization of a high speed PMSM for high performance applications. *IEEE Trans. Magn.* 54(11), 8106405 (2018)
11. Du, G., et al.: Multiphysics design and multiobjective optimization for high-speed permanent magnet machines. *IEEE Trans. Transp. Electr.* 6(3), 1084–1092 (2020)
12. Mack, Y., et al.: Surrogate model-based optimization framework: a case study in aerospace design. *Evol. Comput. Dyn. Uncertain Environ.* 51, 323–342 (2007)
13. Song, X., et al.: A radial basis function-based multi-fidelity surrogate model: exploring correlation between high-fidelity and low-fidelity models. *Struct. Multidiscip. Optim.* 60(3), 965–981 (2019)
14. Song, X., et al.: An advanced and robust ensemble surrogate model: extended adaptive hybrid functions. *J. Mech. Des.* 140(4), 041402 (2018)
15. Lim, D.-K., et al.: A novel surrogate-assisted multi-objective optimization algorithm for an electromagnetic machine design. *IEEE Trans. Magn.* 51(3), 1–4 (2015)
16. Uzhegov, N., et al.: Multidisciplinary design process of a 6-slot 2-pole high-speed permanent-magnet synchronous machine. *IEEE Trans. Ind. Electron.* 63(2), 784–795 (2016)
17. Tan, Z., et al.: DFIG machine design for maximizing power output based on surrogate optimization algorithm. *IEEE Trans. Energy Convers.* 30(3), 1154–1162 (2015)
18. Bu, J.-G., et al.: Optimization for airgap flux density waveform of flywheel motor using NSGA-2 and Kriging model based on MaxPro design. *IEEE Trans. Magn.* 53(8), 8203607 (2017)
19. Fang, H., et al.: Rotor design and eddy-current loss suppression for high-speed machines with a solid-PM rotor. *IEEE Trans. Ind. Appl.* 55(1), 448–457 (2018)
20. Song, T., et al.: Multi-physics and multi-objective optimisation design of interior permanent magnet synchronous motor for electric vehicles. *IET Electr. Power Appl.* 14(11), 2243–2254 (2020)
21. Zheng, J., et al.: Sleeve design of permanent-magnet machine for low rotor losses. *Chin. J. Electr. Eng.* 6(4), 86–96 (2020)
22. Guo, H., Qian, H.: Robust design for reducing torque ripple in permanent magnet synchronous motor. *Proc. CSEE.* 32(24), 88–95 (2012)
23. Lv, L., et al.: A fast-converging ensemble infilling approach balancing global exploration and local exploitation: the Go-Inspired Hybrid Infilling Strategy. *J. Mech. Des.* 142(2), 1–13 (2020)
24. Parnianifard, A., et al.: Kriging-assisted robust black-box simulation optimization in direct speed control of DC motor under uncertainty. *IEEE Trans. Magn.* 54(7), 4900210 (2018)
25. Yan, W., et al.: Design and multi-objective optimisation of switched reluctance machine with iron loss. *IET Electr. Power Appl.* 13(4), 435–444 (2019)
26. Kolondzovski, Z., et al.: Rotor dynamic analysis of different rotor structures for high-speed permanent-magnet electrical machines. *IET Electr. Power Appl.* 4(7), 516–524 (2010)

How to cite this article: Dai, R., et al.: Multi-objective optimisation of the HSPMM rotor based on the multi-physics surrogate model. *IET Electr. Power Appl.* 15(12), 1616–1629 (2021). <https://doi.org/10.1049/elp2.12126>